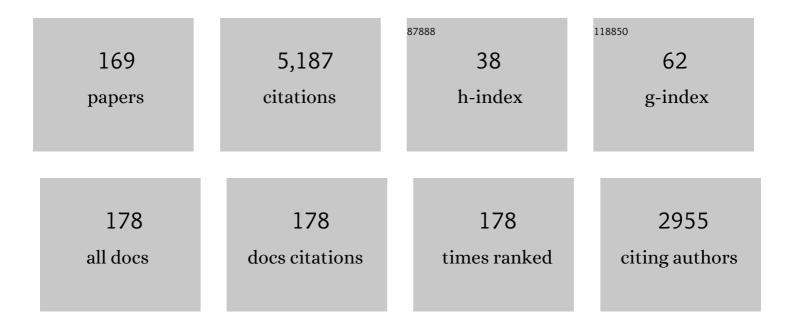
List of Publications by Year in descending order

Source: https://exaly.com/author-pdf/9371954/publications.pdf Version: 2024-02-01



#	Article	IF	CITATIONS
1	Resolving three-dimensional surface displacements from InSAR measurements: A review. Earth-Science Reviews, 2014, 133, 1-17.	9.1	361
2	Mapping ground surface deformation using temporarily coherent point SAR interferometry: Application to Los Angeles Basin. Remote Sensing of Environment, 2012, 117, 429-439.	11.0	164
3	Slope deformation prior to Zhouqu, China landslide from InSAR time series analysis. Remote Sensing of Environment, 2015, 156, 45-57.	11.0	148
4	Glacier mass balance in the Qinghai–Tibet Plateau and its surroundings from the mid-1970s to 2000 based on Hexagon KH-9 and SRTM DEMs. Remote Sensing of Environment, 2018, 210, 96-112.	11.0	147
5	Atmospheric Effects on InSAR Measurements and Their Mitigation. Sensors, 2008, 8, 5426-5448.	3.8	139
6	Monitoring surface deformation over permafrost with an improved SBAS-InSAR algorithm: With emphasis on climatic factors modeling. Remote Sensing of Environment, 2016, 184, 276-287.	11.0	131
7	Slight glacier mass loss in the Karakoram region during the 1970s to 2000 revealed by KH-9 images and SRTM DEM. Journal of Glaciology, 2017, 63, 331-342.	2.2	96
8	3D coseismic Displacement of 2010 Darfield, New Zealand earthquake estimated from multi-aperture InSAR and D-InSAR measurements. Journal of Geodesy, 2012, 86, 1029-1041.	3.6	95
9	Coseismic fault slip of the 2008 M <sub>w</sub> 7.9 Wenchuan earthquake estimated from InSAR and GPS measurements. Geophysical Research Letters, 2010, 37, .	4.0	94
10	Ground Subsidence Monitoring in Hong Kong with Satellite SAR Interferometry. Photogrammetric Engineering and Remote Sensing, 2004, 70, 1151-1156.	0.6	93
11	Deriving Dynamic Subsidence of Coal Mining Areas Using InSAR and Logistic Model. Remote Sensing, 2017, 9, 125.	4.0	92
12	Retrieving three-dimensional displacement fields of mining areas from a single InSAR pair. Journal of Geodesy, 2015, 89, 17-32.	3.6	84
13	Improved filtering parameter determination for the Goldstein radar interferogram filter. ISPRS Journal of Photogrammetry and Remote Sensing, 2008, 63, 621-634.	11.1	83
14	Transpressional Rupture Cascade of the 2016 M <sub>w</sub> 7.8 Kaikoura Earthquake, New Zealand. Journal of Geophysical Research: Solid Earth, 2018, 123, 2396-2409.	3.4	83
15	Coastal Subsidence Monitoring Associated with Land Reclamation Using the Point Target Based SBAS-InSAR Method: A Case Study of Shenzhen, China. Remote Sensing, 2016, 8, 652.	4.0	78
16	Time-series InSAR ground deformation monitoring: Atmospheric delay modeling and estimating. Earth-Science Reviews, 2019, 192, 258-284.	9.1	78
17	A Novel Multitemporal InSAR Model for Joint Estimation of Deformation Rates and Orbital Errors. IEEE Transactions on Geoscience and Remote Sensing, 2014, 52, 3529-3540.	6.3	77
18	Use of SAR/InSAR in Mining Deformation Monitoring, Parameter Inversion, and Forward Predictions: A Review. IEEE Geoscience and Remote Sensing Magazine, 2020, 8, 71-90.	9.6	72

#	Article	IF	CITATIONS
19	Geodetic model of the 2015 April 25 Mw 7.8 Gorkha Nepal Earthquake and Mw 7.3 aftershock estimated from InSAR and GPS data. Geophysical Journal International, 2015, 203, 896-900.	2.4	71
20	Toward full exploitation of coherent and incoherent information in Sentinelâ€1 TOPS data for retrieving surface displacement: Application to the 2016 Kumamoto (Japan) earthquake. Geophysical Research Letters, 2017, 44, 1758-1767.	4.0	68
21	InSAR analysis of surface deformation over permafrost to estimate active layer thickness based on one-dimensional heat transfer model of soils. Scientific Reports, 2015, 5, 15542.	3.3	66
22	InSAR-Based Model Parameter Estimation of Probability Integral Method and Its Application for Predicting Mining-Induced Horizontal and Vertical Displacements. IEEE Transactions on Geoscience and Remote Sensing, 2016, 54, 4818-4832.	6.3	64
23	Three-Dimensional Surface Displacements From InSAR and GPS Measurements With Variance Component Estimation. IEEE Geoscience and Remote Sensing Letters, 2012, 9, 754-758.	3.1	62
24	Review of the SBAS InSAR Time-series algorithms, applications, and challenges. Geodesy and Geodynamics, 2022, 13, 114-126.	2.2	61
25	Correcting atmospheric effects on InSAR with MERIS water vapour data and elevation-dependent interpolation model. Geophysical Journal International, 2012, 189, 898-910.	2.4	60
26	Hybrid Approach for Unbiased Coherence Estimation for Multitemporal InSAR. IEEE Transactions on Geoscience and Remote Sensing, 2014, 52, 2459-2473.	6.3	59
27	Deriving Spatio-Temporal Development of Ground Subsidence Due to Subway Construction and Operation in Delta Regions with PS-InSAR Data: A Case Study in Guangzhou, China. Remote Sensing, 2017, 9, 1004.	4.0	55
28	Kalman-Filter-Based Approach for Multisensor, Multitrack, and Multitemporal InSAR. IEEE Transactions on Geoscience and Remote Sensing, 2013, 51, 4226-4239.	6.3	53
29	Inferring three-dimensional surface displacement field by combining SAR interferometric phase and amplitude information of ascending and descending orbits. Science China Earth Sciences, 2010, 53, 550-560.	5.2	48
30	3-D movement mapping of the alpine glacier in Qinghai-Tibetan Plateau by integrating D-InSAR, MAI and Offset-Tracking: Case study of the Dongkemadi Glacier. Global and Planetary Change, 2014, 118, 62-68.	3.5	48
31	A Method for Measuring 3-D Surface Deformations With InSAR Based on Strain Model and Variance Component Estimation. IEEE Transactions on Geoscience and Remote Sensing, 2018, 56, 239-250.	6.3	48
32	Modeling atmospheric effects on InSAR with meteorological and continuous GPS observations: algorithms and some test results. Journal of Atmospheric and Solar-Terrestrial Physics, 2004, 66, 907-917.	1.6	47
33	Quantifying glacier mass change and its contribution to lake growths in central Kunlun during 2000–2015 from multi-source remote sensing data. Journal of Hydrology, 2019, 570, 38-50.	5.4	47
34	Pre- and post-failure spatial-temporal deformation pattern of the Baige landslide retrieved from multiple radar and optical satellite images. Engineering Geology, 2020, 279, 105880.	6.3	46
35	A Refined Strategy for Removing Composite Errors of SAR Interferogram. IEEE Geoscience and Remote Sensing Letters, 2014, 11, 143-147.	3.1	45
36	Locating and defining underground goaf caused by coal mining from space-borne SAR interferometry. ISPRS Journal of Photogrammetry and Remote Sensing, 2018, 135, 112-126.	11.1	43

#	Article	IF	CITATIONS
37	Early 21st century glacier thickness changes in the Central Tien Shan. Remote Sensing of Environment, 2017, 192, 12-29.	11.0	42
38	Least Squares-Based Filter for Remote SensingImage Noise Reduction. IEEE Transactions on Geoscience and Remote Sensing, 2008, 46, 2044-2049.	6.3	41
39	Modeling minimum and maximum detectable deformation gradients of interferometric SAR measurements. International Journal of Applied Earth Observation and Geoinformation, 2011, 13, 766-777.	2.8	39
40	Calibration of an InSAR-Derived Coseimic Deformation Map Associated With the 2011 Mw-9.0 Tohoku-Oki Earthquake. IEEE Geoscience and Remote Sensing Letters, 2012, 9, 302-306.	3.1	39
41	An Extension of the InSAR-Based Probability Integral Method and Its Application for Predicting 3-D Mining-Induced Displacements Under Different Extraction Conditions. IEEE Transactions on Geoscience and Remote Sensing, 2017, 55, 3835-3845.	6.3	38
42	Modeling of atmospheric effects on InSAR measurements by incorporating terrain elevation information. Journal of Atmospheric and Solar-Terrestrial Physics, 2006, 68, 1189-1194.	1.6	37
43	Investigating mountain glacier motion with the method of SAR intensity-tracking: Removal of topographic effects and analysis of the dynamic patterns. Earth-Science Reviews, 2014, 138, 179-195.	9.1	37
44	Coseismic and Early Postseismic Slip Models of the 2021 Mw 7.4 Maduo Earthquake (Western China) Estimated by Spaceâ€Based Geodetic Data. Geophysical Research Letters, 2021, 48, .	4.0	36
45	Vertical and horizontal displacements of Los Angeles from InSAR and GPS time series analysis: Resolving tectonic and anthropogenic motions. Journal of Geodynamics, 2016, 99, 27-38.	1.6	35
46	Stochastic modeling for time series InSAR: with emphasis on atmospheric effects. Journal of Geodesy, 2018, 92, 185-204.	3.6	35
47	Retrieving 3-D Large Displacements of Mining Areas from a Single Amplitude Pair of SAR Using Offset Tracking. Remote Sensing, 2017, 9, 338.	4.0	34
48	Source parameters of the 2014 Mw 6.1 South Napa earthquake estimated from the Sentinel 1A, COSMO-SkyMed and GPS data. Tectonophysics, 2015, 655, 139-146.	2.2	32
49	Spatio-Temporal Error Sources Analysis and Accuracy Improvement in Landsat 8 Image Ground Displacement Measurements. Remote Sensing, 2016, 8, 937.	4.0	32
50	On the Accuracy of Topographic Residuals Retrieved by MTInSAR. IEEE Transactions on Geoscience and Remote Sensing, 2017, 55, 1053-1065.	6.3	31
51	Deriving time-series three-dimensional displacements of mining areas from a single-geometry InSAR dataset. Journal of Geodesy, 2018, 92, 529-544.	3.6	31
52	Estimating three-dimensional coseismic deformations with the SM-VCE method based on heterogeneous SAR observations: Selection of homogeneous points and analysis of observation combinations. Remote Sensing of Environment, 2021, 255, 112298.	11.0	31
53	Interpolating atmospheric water vapor delay by incorporating terrain elevation information. Journal of Geodesy, 2011, 85, 555-564.	3.6	30
54	The potential of more accurate InSAR covariance matrix estimation for land cover mapping. ISPRS Journal of Photogrammetry and Remote Sensing, 2017, 126, 120-128.	11.1	30

#	Article	IF	CITATIONS
55	Which Fault Segments Ruptured in the 2008 Wenchuan Earthquake and Which Did Not? New Evidence from Nearâ€Fault 3D Surface Displacements Derived from SAR Image Offsets. Bulletin of the Seismological Society of America, 2017, 107, 1185-1200.	2.3	29
56	Source parameters and triggering links of the earthquake sequence in central Italy from 2009 to 2016 analyzed with GPS and InSAR data. Tectonophysics, 2018, 744, 285-295.	2.2	29
57	Quantifying the spatio-temporal patterns of dune migration near Minqin Oasis in northwestern China with time series of Landsat-8 and Sentinel-2 observations. Remote Sensing of Environment, 2020, 236, 111498.	11.0	29
58	Atmospheric effects on repeat-pass InSAR measurements over Shanghai region. Journal of Atmospheric and Solar-Terrestrial Physics, 2007, 69, 1344-1356.	1.6	28
59	An improved geodetic source model for the 1999 <i>M</i> <sub>w</sub> 6.3 Chamoli earthquake, India. Geophysical Journal International, 2016, 205, 236-242.	2.4	28
60	An InSAR-Based Temporal Probability Integral Method and its Application for Predicting Mining-Induced Dynamic Deformations and Assessing Progressive Damage to Surface Buildings. IEEE Journal of Selected Topics in Applied Earth Observations and Remote Sensing, 2018, 11, 472-484.	4.9	28
61	Derivation of 3-D coseismic surface displacement fields for the 2011 Mw 9.0 Tohoku-Oki earthquake from InSAR and GPS measurements. Geophysical Journal International, 2013, 192, 573-585.	2.4	27
62	Crosswind stability of high-speed trains in special cuts. Journal of Central South University, 2015, 22, 2849-2856.	3.0	27
63	Recent Landslide Movement in Tsaoling, Taiwan Tracked by TerraSAR-X/TanDEM-X DEM Time Series. Remote Sensing, 2017, 9, 353.	4.0	27
64	Deriving a time series of 3D glacier motion to investigate interactions of a large mountain glacial system with its glacial lake: Use of Synthetic Aperture Radar Pixel Offset-Small Baseline Subset technique. Journal of Hydrology, 2018, 559, 596-608.	5.4	27
65	Complete Threeâ€Dimensional Coseismic Deformation Field of the 2016 Central Tottori Earthquake by Integrating Left―and Right‣ooking InSAR Observations With the Improved SMâ€VCE Method. Journal of Geophysical Research: Solid Earth, 2019, 124, 12099-12115.	3.4	27
66	Source parameters and slip distribution of the 2018 M 7.5 Palu, Indonesia earthquake estimated from space-based geodesy. Tectonophysics, 2019, 772, 228216.	2.2	27
67	Complete three-dimensional coseismic displacements due to the 2021 Maduo earthquake in Qinghai Province, China from Sentinel-1 and ALOS-2 SAR images. Science China Earth Sciences, 2022, 65, 687-697.	5.2	27
68	Pre- and co-seismic ground deformations of the 1999 Chi-Chi, Taiwan earthquake, measured with SAR interferometry. Computers and Geosciences, 2004, 30, 333-343.	4.2	26
69	Correcting ionospheric effects and monitoring two-dimensional displacement fields with multiple-aperture InSAR technology with application to the Yushu earthquake. Science China Earth Sciences, 2012, 55, 1961-1971.	5.2	26
70	Investigating the Ground Deformation and Source Model of the Yangbajing Geothermal Field in Tibet, China with the WLS InSAR Technique. Remote Sensing, 2016, 8, 191.	4.0	26
71	Understanding Land Subsidence Along the Coastal Areas of Guangdong, China, by Analyzing Multi-Track MTInSAR Data. Remote Sensing, 2020, 12, 299.	4.0	25
72	InSAR Coherence Estimation for Small Data Sets and Its Impact on Temporal Decorrelation Extraction. IEEE Transactions on Geoscience and Remote Sensing, 2014, 52, 6584-6596.	6.3	24

#	Article	IF	CITATIONS
73	Displacement history and potential triggering factors of Baige landslides, China revealed by optical imagery time series. Remote Sensing of Environment, 2021, 254, 112253.	11.0	23
74	Shortcomings of InSAR for studying megathrust earthquakes: The case of the M <sub>w</sub> 9.0 Tohokuâ€Oki earthquake. Geophysical Research Letters, 2012, 39, .	4.0	22
75	Advanced InSAR Tropospheric Corrections From Global Atmospheric Models that Incorporate Spatial Stochastic Properties of the Troposphere. Journal of Geophysical Research: Solid Earth, 2021, 126, e2020JB020952.	3.4	22
76	Potential of geosynchronous SAR interferometric measurements in estimating three-dimensional surface displacements. Science China Information Sciences, 2017, 60, 1.	4.3	21
77	Two-dimensional Co-Seismic Surface Displacements Field of the Chi-Chi Earthquake Inferred from SAR Image Matching. Sensors, 2008, 8, 6484-6495.	3.8	20
78	Spatial–temporal surface deformation of Los Angeles over 2003–2007 from weighted least squares DInSAR. International Journal of Applied Earth Observation and Geoinformation, 2013, 21, 484-492.	2.8	20
79	Coseismic Deformation of the 2015 <i>M</i> <sub>w</sub> Â6.4 Pishan, China, Earthquake Estimated from Sentinelâ€IA and ALOS2 Data. Seismological Research Letters, 2016, 87, 800-806.	1.9	20
80	Estimation of 3-D Surface Displacement Based on InSAR and Deformation Modeling. IEEE Transactions on Geoscience and Remote Sensing, 2017, 55, 2007-2016.	6.3	20
81	Geodetic glacier mass balance (1975–1999) in the central Pamir using the SRTM DEM and KH-9 imagery. Journal of Glaciology, 2019, 65, 309-320.	2.2	20
82	The joint driving effects of climate and weather changes caused the Chamoli glacier-rock avalanche in the high altitudes of the India Himalaya. Science China Earth Sciences, 2021, 64, 1909-1921.	5.2	20
83	Ground settlement of Chek Lap Kok Airport, Hong Kong, detected by satellite synthetic aperture radar interferometry. Science Bulletin, 2001, 46, 1778-1782.	1.7	19
84	Deriving surface motion of mountain glaciers in the Tuomuer-Khan Tengri Mountain Ranges from PALSAR images. Global and Planetary Change, 2013, 101, 61-71.	3.5	19
85	The Surge of the Hispar Glacier, Central Karakoram: SAR 3â€Ð Flow Velocity Time Series and Thickness Changes. Journal of Geophysical Research: Solid Earth, 2020, 125, e2019JB018945.	3.4	19
86	Three-Dimensional Surface Displacements of the 8 January 2022 Mw6.7 Menyuan Earthquake, China from Sentinel-1 and ALOS-2 SAR Observations. Remote Sensing, 2022, 14, 1404.	4.0	19
87	The Improvement for Baran Phase Filter Derived From Unbiased InSAR Coherence. IEEE Journal of Selected Topics in Applied Earth Observations and Remote Sensing, 2014, 7, 3002-3010.	4.9	18
88	Monitoring the land subsidence with persistent scatterer interferometry in Nansha District, Guangdong, China. Natural Hazards, 2015, 75, 2947-2964.	3.4	18
89	Continent-Wide 2-D Co-Seismic Deformation of the 2015 Mw 8.3 Illapel, Chile Earthquake Derived from Sentinel-1A Data: Correction of Azimuth Co-Registration Error. Remote Sensing, 2016, 8, 376.	4.0	18
90	An Alternative Method for Estimating 3-D Large Displacements of Mining Areas from a Single SAR Amplitude Pair Using Offset Tracking. IEEE Transactions on Geoscience and Remote Sensing, 2018, 56, 3645-3656.	6.3	18

#	Article	IF	CITATIONS
91	Kinematic Parameter Inversion of the Slumgullion Landslide Using the Time Series Offset Tracking Method With UAVSAR Data. Journal of Geophysical Research: Solid Earth, 2018, 123, 8110-8124.	3.4	18
92	Effects of External Digital Elevation Model Inaccuracy on StaMPS-PS Processing: A Case Study in Shenzhen, China. Remote Sensing, 2017, 9, 1115.	4.0	17
93	Time-Series 3-D Mining-Induced Large Displacement Modeling and Robust Estimation From a Single-Geometry SAR Amplitude Data Set. IEEE Transactions on Geoscience and Remote Sensing, 2018, 56, 3600-3610.	6.3	16
94	Filtering method for SAR interferograms with strong noise. International Journal of Remote Sensing, 2006, 27, 2991-3000.	2.9	15
95	Monitoring the Degradation of Island Permafrost Using Time-Series InSAR Technique: A Case Study of Heihe, China. Sensors, 2019, 19, 1364.	3.8	15
96	A New Weighting Method by Considering the Physical Characteristics of Atmospheric Turbulence and Decorrelation Noise in SBAS-InSAR. Remote Sensing, 2020, 12, 2557.	4.0	14
97	SAR Interferometric Baseline Refinement Based on Flat-Earth Phase without a Ground Control Point. Remote Sensing, 2020, 12, 233.	4.0	14
98	An Improved Method for Automatic Identification and Assessment of Potential Geohazards Based on MT-InSAR Measurements. Remote Sensing, 2021, 13, 3490.	4.0	14
99	Retrieving the displacements of the Hutubi (China) underground gas storage during 2003–2020 from multi-track InSAR. Remote Sensing of Environment, 2022, 268, 112768.	11.0	14
100	Improved Goldstein filter for InSAR noise reduction based on local SNR. Journal of Central South University, 2013, 20, 1896-1903.	3.0	13
101	Characterizing sudden geo-hazards in mountainous areas by D-InSAR with an enhancement of topographic error correction. Natural Hazards, 2015, 75, 2343-2356.	3.4	13
102	Subsidence Evolution of the Leizhou Peninsula, China, Based on InSAR Observation from 1992 to 2010. Applied Sciences (Switzerland), 2017, 7, 466.	2.5	13
103	Retrieving three-dimensional coseismic displacements of the 2008 Gaize, Tibet earthquake from multi-path interferometric phase analysis. Natural Hazards, 2014, 73, 1311-1322.	3.4	12
104	An Optimized Choice of UCPML to Truncate Lattices With Rotated Staggered Grid Scheme for Ground Penetrating Radar Simulation. IEEE Transactions on Geoscience and Remote Sensing, 2019, 57, 8695-8706.	6.3	12
105	Anisotropy of atmospheric delay in InSAR and its effect on InSAR atmospheric correction. Journal of Geodesy, 2019, 93, 241-265.	3.6	12
106	Kinematic Coregistration of Sentinel-1 TOPSAR Images Based on Sequential Least Squares Adjustment. IEEE Journal of Selected Topics in Applied Earth Observations and Remote Sensing, 2020, 13, 3083-3093.	4.9	12
107	Investigating the Recent Surge in the Monomah Glacier, Central Kunlun Mountain Range with Multiple Sources of Remote Sensing Data. Remote Sensing, 2020, 12, 966.	4.0	12
108	The 3-D surface deformation, coseismic fault slip and after-slip of the 2010 Mw6.9 Yushu earthquake, Tibet, China. Journal of Asian Earth Sciences, 2016, 124, 260-268.	2.3	11

#	Article	IF	CITATIONS
109	Anomalous Glacier Changes in the Southeast of Tuomuerâ€Khan Tengri Mountain Ranges, Central Tianshan. Journal of Geophysical Research D: Atmospheres, 2018, 123, 6840-6863.	3.3	11
110	Fusing adjacent-track InSAR datasets to densify the temporal resolution of time-series 3-D displacement estimation over mining areas with a prior deformation model and a generalized weighting least-squares method. Journal of Geodesy, 2020, 94, 1.	3.6	11
111	A Strainâ€Model Based InSAR Time Series Method and Its Application to The Geysers Geothermal Field, California. Journal of Geophysical Research: Solid Earth, 2021, 126, e2021JB021939.	3.4	11
112	Underlying topography extraction over forest areas from multi-baseline PolInSAR data. Journal of Geodesy, 2018, 92, 727-741.	3.6	10
113	Investigating the bias of TanDEM-X digital elevation models of glaciers on the Tibetan Plateau: impacting factors and potential effects on geodetic mass-balance measurements. Journal of Glaciology, 0, , 1-14.	2.2	10
114	A Novel Vessel Velocity Estimation Method Using Dual-Platform TerraSAR-X and TanDEM-X Full Polarimetric SAR Data in Pursuit Monostatic Mode. IEEE Transactions on Geoscience and Remote Sensing, 2019, 57, 6130-6144.	6.3	9
115	An Improved Quadtree Sampling Method for InSAR Seismic Deformation Inversion. Remote Sensing, 2021, 13, 1678.	4.0	9
116	Estimation of subcanopy topography based on single-baseline TanDEM-X InSAR data. Journal of Geodesy, 2021, 95, 1.	3.6	9
117	Comparative Study of Empirical Tropospheric Models for the Hong Kong Region. Survey Review, 2008, 40, 328-341.	1.2	8
118	Coseismic slip distribution of 2009 L'Aquila earthquake derived from InSAR and GPS data. Journal of Central South University, 2012, 19, 244-251.	3.0	8
119	Improved fast mean shift algorithm for remote sensing image segmentation. IET Image Processing, 2015, 9, 389-394.	2.5	8
120	High-Resolution Three-Dimensional Displacement Retrieval of Mining Areas From a Single SAR Amplitude Pair Using the SPIKE Algorithm. IEEE Journal of Selected Topics in Applied Earth Observations and Remote Sensing, 2018, 11, 3782-3793.	4.9	8
121	Mapping three-dimensional co-seismic surface deformations associated with the 2015 MW7.2 Murghab earthquake based on InSAR and characteristics of crustal strain. Science China Earth Sciences, 2018, 61, 1451-1466.	5.2	8
122	Spatially Heterogeneous Land Surface Deformation Data Fusion Method Based on an Enhanced Spatio-Temporal Random Effect Model. Remote Sensing, 2019, 11, 1084.	4.0	8
123	A Method for Surface Water Body Detection and DEM Generation With Multigeometry TanDEM-X Data. IEEE Journal of Selected Topics in Applied Earth Observations and Remote Sensing, 2019, 12, 151-161.	4.9	8
124	Correction of Time-Varying Baseline Errors Based on Multibaseline Airborne Interferometric Data Without High-Precision DEMs. IEEE Transactions on Geoscience and Remote Sensing, 2021, 59, 9307-9318.	6.3	8
125	Mapping Complete Three-Dimensional Ice Velocities by Integrating Multi-Baseline and Multi-Aperture InSAR Measurements: A Case Study of the Grove Mountains Area, East Antarctic. Remote Sensing, 2021, 13, 643.	4.0	8
126	Surface Displacement and Source Model Separation of the Two Strongest Earthquakes During the 2019 Ridgecrest Sequence: Insights From InSAR, GPS, and Optical Data. Journal of Geophysical Research: Solid Earth, 2022, 127, .	3.4	8

#	Article	IF	CITATIONS
127	Mitigation of time-series InSAR turbulent atmospheric phase noise: A review. Geodesy and Geodynamics, 2022, 13, 93-103.	2.2	8
128	The least-squares estimation of adjustment model constrained by some non-negative parameters. Survey Review, 2010, 42, 62-71.	1.2	7
129	Generalized functional model of maximum and minimum detectable deformation gradient for PALSAR interferometry. Transactions of Nonferrous Metals Society of China, 2014, 24, 824-832.	4.2	7
130	Blind thrust rupture of the 2015 Mw 6.4 Pishan earthquake in the Northwest Tibetan Plateau by joint inversion of InSAR and seismic data. Journal of Asian Earth Sciences, 2016, 132, 118-128.	2.3	7
131	Deriving 3-D Time-Series Ground Deformations Induced by Underground Fluid Flows with InSAR: Case Study of Sebei Gas Fields, China. Remote Sensing, 2017, 9, 1129.	4.0	7
132	Mapping ground displacement by a multiple phase difference-based InSAR approach: with stochastic model estimation and turbulent troposphere mitigation. Journal of Geodesy, 2019, 93, 1313-1333.	3.6	7
133	Block PS-InSAR ground deformation estimation for large-scale areas based on network adjustment. Journal of Geodesy, 2021, 95, 1.	3.6	7
134	Surface deformation evolution in the Pearl River Delta between 2006 and 2011 derived from the ALOS1/PALSAR images. Earth, Planets and Space, 2020, 72, .	2.5	7
135	Quantitative study of atmospheric effects in spaceborne InSAR measurements. Central South University, 2005, 12, 494-498.	0.5	6
136	Six years of land subsidence in shanghai revealed by JERS-1 SAR data. , 2007, , .		6
137	A new moving model test method for the measurement of aerodynamic drag coefficient of high-speed trains based on machine vision. Proceedings of the Institution of Mechanical Engineers, Part F: Journal of Rail and Rapid Transit, 2018, 232, 1425-1436.	2.0	6
138	CRInSAR Using Two-Step LAMBDA Algorithm for Nonlinear Deformation Estimation: Case Study of Monitoring Xiangtan Converter Station, China. IEEE Geoscience and Remote Sensing Letters, 2020, 17, 963-967.	3.1	6
139	Adaptively Selecting Interferograms for SBAS-InSAR Based on Graph Theory and Turbulence Atmosphere. IEEE Access, 2020, 8, 112898-112909.	4.2	6
140	Prediction of Mining-Induced Kinematic 3-D Displacements From InSAR Using a Weibull Model and a Kalman Filter. IEEE Transactions on Geoscience and Remote Sensing, 2022, 60, 1-12.	6.3	6
141	Highâ€Resolution Water Vapor Maps Obtained by Merging Interferometric Synthetic Aperture Radar and GPS Measurements. Journal of Geophysical Research D: Atmospheres, 2021, 126, .	3.3	6
142	Orbit error removal in InSAR/MTInSAR with a patch-based polynomial model. International Journal of Applied Earth Observation and Geoinformation, 2021, 102, 102438.	2.8	6
143	A Phase Optimization Method for DS-InSAR Based on SKP Decomposition From Quad-Polarized Data. IEEE Geoscience and Remote Sensing Letters, 2022, 19, 1-5.	3.1	6
144	Change detection, risk assessment and mass balance of mobile dune fields near Dunhuang Oasis with optical imagery and global terrain datasets. International Journal of Digital Earth, 2020, 13, 1604-1623.	3.9	6

#	Article	IF	CITATIONS
145	An Improved Phase Unwrapping Method Based on Hierarchical Networking and Constrained Adjustment. Remote Sensing, 2021, 13, 4193.	4.0	6
146	A Block Ramp Errors Correction Method of Planet Subpixel Offset: Application to the 2018 Mw 7.5 Palu Earthquake, Indonesia. IEEE Access, 2019, 7, 174924-174931.	4.2	5
147	A novel method for determining the anisotropy of geophysical parameters: unit range variation increment (URVI). Applied Geophysics, 2014, 11, 340-349.	0.6	4
148	High-Rise Building Layover Exploitation with Non-Local Frequency Estimation in SAR Interferograms. Remote Sensing, 2017, 9, 579.	4.0	4
149	Non-differential water vapor estimation from SBAS-InSAR. Journal of Atmospheric and Solar-Terrestrial Physics, 2020, 204, 105284.	1.6	4
150	Derivation of high-quality three-dimensional surface deformation velocities through multi-source point cloud fusion: Application to Kīlauea volcano. International Journal of Applied Earth Observation and Geoinformation, 2021, 95, 102270.	2.8	4
151	Monitoring Bridge Vibrations Based on GBSAR and Validation by High-Rate GPS Measurements. IEEE Journal of Selected Topics in Applied Earth Observations and Remote Sensing, 2021, 14, 5572-5580.	4.9	4
152	Helmert Variance Component Estimation-based Vondrak Filter and its Application in GPS Multipath Error Mitigation. , 2008, , 287-292.		4
153	Dynamic Estimation of Multi-Dimensional Deformation Time Series From InSAR Based on Kalman Filter and Strain Model. IEEE Transactions on Geoscience and Remote Sensing, 2022, 60, 1-16.	6.3	4
154	Settlement Prediction of Reclaimed Coastal Airports with InSAR Observation: A Case Study of the Xiamen Xiang'an International Airport, China. Remote Sensing, 2022, 14, 3081.	4.0	4
155	SAR interferogram filtering with 2D Vondrak filter. , 0, , .		3
156	Study on Ocean Wind Vector Retrieval from ERSâ€⊋ SAR Image. Chinese Journal of Geophysics, 2007, 50, 1466-1473.	0.2	3
157	Resolving 3-D Mining Displacements From Multi-Track InSAR by Incorporating With a Prior Model: The Dynamic Changes and Adaptive Estimation of the Model Parameters. IEEE Transactions on Geoscience and Remote Sensing, 2022, 60, 1-10.	6.3	3
158	Evolution of geodetic mass balance over the largest lake-terminating glacier in the Tibetan Plateau with a revised radar penetration depth based on multi-source high-resolution satellite data. Remote Sensing of Environment, 2022, 275, 113029.	11.0	3
159	Hazard development mechanism and deformation estimation of water solution mining area. Central South University, 2006, 13, 738-742.	0.5	2
160	Continued Monitoring and Modeling of Xingfeng Solid Waste Landfill Settlement, China, Based on Multiplatform SAR Images. Remote Sensing, 2021, 13, 3286.	4.0	2
161	Monitoring of Surface Subsidence of the Mining Area Based on SBAS. Journal of Computers, 2014, 9, .	0.4	2
162	SCGM(1,m)c model with time-lag and its application in deformation analysis. Central South University, 2001, 8, 40-44.	0.5	1

#	Article	IF	CITATIONS
163	Magnitude and Extent of Six Years of Land Subsidence in Shanghai Revealed by JERS-1 SAR Data. , 0, , .		1
164	Analysis on the Application of GPS in Hull Installment and Marine Monitoring. Applied Mechanics and Materials, 0, 55-57, 1111-1115.	0.2	1
165	Discussion on GPS-RTK Using in Undersea Topographic Survey. Key Engineering Materials, 2011, 467-469, 829-834.	0.4	1
166	Quantifying Dynamic Characteristics of Dune Migration in Northwestern China with Multitemporal Optical Satellite Observations. , 2019, , .		1
167	Modeling of atmospheric effects on InSAR by incorporating terrain elevation information. , 0, , .		0
168	The Application of GPS Using in Steel Sheet Pile Implementing the Localization on the Sea Surveying. Advanced Materials Research, 0, 204-210, 741-745.	0.3	0
169	Spatial statistics of atmospheric signal in repeat-pass InSAR. , 2014, , .		ο